International Journal of Nanomedicine

Dovepress
open access to scientific and medical research

Open Access Full Text Article

ORIGINAL RESEARCH

Alendronate Functionalized Bone-Targeting Pomolic Acid Liposomes Restore Bone Homeostasis for Osteoporosis Treatment

Demeng Xia[1,2,*], Qingqing Qian[1,*], Sheng Wang[3,*], Xiao Dong[4], Ying Liu[5]

[1]Department of Pharmacy, The Fifth People's Hospital of Shanghai, Fudan University, Shanghai, 200240, People's Republic of China; [2]Department of Pharmacy, Seventh People's Hospital of Shanghai University of Traditional Chinese Medicine, Shanghai, 200120, People's Republic of China; [3]Department of Traumatic Orthopedics, Shanghai Fourth People's Hospital, School of Medicine, Tongji University, Shanghai, 200434, People's Republic of China; [4]School of Medicine, Shanghai University, Shanghai, 200444, People's Republic of China; [5]Institute of Translational Medicine, Shanghai University, Shanghai, 200444, People's Republic of China

*These authors contributed equally to this work

Correspondence: Ying Liu; Xiao Dong, Email liuchanger1984@163.com; dong-xiao@shu.edu.cn

Introduction: Osteoporosis, characterized by dysregulation of osteoclastic bone resorption and osteoblastic bone formation, severely threatens human health during aging. However, there is still no good therapy for osteoporosis, so this direction requires our continuous attention, and there is an urgent need for new drugs to solve this problem.

Methods: Traditional Chinese Medicine Salvia divinorum monomer pomolic acid (PA) could effectively inhibit osteoclastogenesis and ovariectomized osteoporosis. However, its poor solubility and lack of targeting severely limits its further application. A novel bone-targeting nanomedicine (PA@TLipo) has been developed to reconstruct the osteoporotic microenvironment by encapsulating pomolic acid in alendronate-functionalized liposomes. Through a series of operations such as synthesis, purification, encapsulation, and labeling, the PA@TLipo have been prepared. Moreover, the cytotoxicity, bone targeting and anti-osteoporosis effect was verified by cell and animal experiments.

Results: In the aspect of targeting, the PA@TLipo can effectively aggregate on the bone tissue to reduce bone loss, and in terms of toxicity, PA@TLipo could increase the bone target ability in comparison to nontargeted liposome, thereby mitigating systemic cytotoxicity. Moreover, PA@TLipo inhibited osteoclast formation and bone resorption in vitro and reduced bone loss in ovariectomy-induced osteoporotic mice.

Conclusion: In this study, a novel therapeutic agent was designed and constructed to treat osteoporosis, consisting of a liposome material as the drug pocket, PA as the anti-osteoporosis drug, and ALN as the bone-targeting molecule. And our study is the first to employ a bone-targeted delivery system to deliver PA for OVX-induced bone loss, providing an innovative solution for treating osteoporosis.

Keywords: bone targeting, alendronate functionalized liposome, pomolic acid, osteoporosis therapy

Introduction

Osteoporosis is a skeletal disorder characterized by the gradual degradation of microstructural integrity in bone tissue, which is accompanied by a reduction in bone mass, heightened bone fragility, and an augmented susceptibility to secondary fractures. This pathological condition is predominantly attributed to the pathological activity of osteoclasts, which are the cells responsible for bone resorption.[1–6] Bisphosphonates, classified as antiresorptive agents, are widely used to treat osteoporosis.[7,8] Nevertheless, prolonged administration of these drugs raises concerns regarding their potential adverse effects, including necrosis, atypical maxillary fractures, and esophageal irritation.[9–12] Therefore, it is beneficial to explore novel therapeutic compounds that offer enhanced efficacy.

Received: 2 February 2024
Accepted: 11 June 2024
Published: 6 August 2024

Salvia divinorum is a famous Traditional Chinese Medicine (TCM) that increases blood flow, regulates menstruation, and relieves pain in the injured area.[13–17] Salvia divinorum has attracted increasing interest because of its proven pharmacological safety as well as its diverse range of biological properties, including antioxidant, anti-inflammatory, and anticancer.[18–23] The active ingredients of Salvia miltiorrhiza inhibit osteoclast formation and bone loss.[24–27] Dihydrotanshinone I attenuates estrogen-deficient osteoporosis by inhibiting the receptor activator of nuclear kappa B ligand (RANKL)-stimulated NF-κB, extracellular signal-regulated kinase (ERK), and nuclear factor of activated T cell cytoplasmic 1 (NFATc1) signaling pathways.[28] Tanshinol, another major water-soluble active component of Salvia miltiorrhiza, has potential therapeutic effects against glucocorticoid-induced osteoporosis in rats.[29] Although these findings have shown promising potential in the prevention and treatment of osteoporosis using Salvia miltiorrhiza, the precise underlying mechanisms remain unexplored.

Through network pharmacology analysis, we screened the active ingredients of Salvia miltiorrhiza for their potential use in the treatment of osteoporosis. Our previous investigation revealed that pomolic acid (PA), derived from Salvia miltiorrhiza triterpenoids, exhibits inhibitory effects on bone resorption in vitro and prevents bone loss in ovariectomized (OVX) mice (unpublished). However, systemic administration without targeted delivery systems necessitates a substantial therapeutic dosage of the drug, potentially leading to elevated off-target effects. Simultaneously, the solubility of pure PA in the human body is relatively limited, thereby presenting a challenge for enhancing PA bioavailability. Hence, it is highly desirable to develop bone-targeted drug delivery systems for osteoporosis therapies.

Alendronate (ALN), an FDA-approved bisphosphonate used in the treatment of osteoporosis, exhibits strong affinity for binding to the bone surface, thus establishing its preferential candidacy as a ligand for targeting bone tissue. In this study, we developed ALN-functionalized bone-targeting PA liposomes (PA@TLipo) for selective osteoporosis therapy (Figure 1). Specifically, an ALN-conjugated PEGylated phospholipid (DSPE-PEG$_{3400}$-ALN) was first synthesized using ALN and DSPE-PEG$_{3400}$-NHS. Osteophilic ALN-modified liposomes were prepared using a thin-film dispersion method. Benefiting from the high binding affinity of ALN to the exposed hydroxyapatite of the bone structure, the

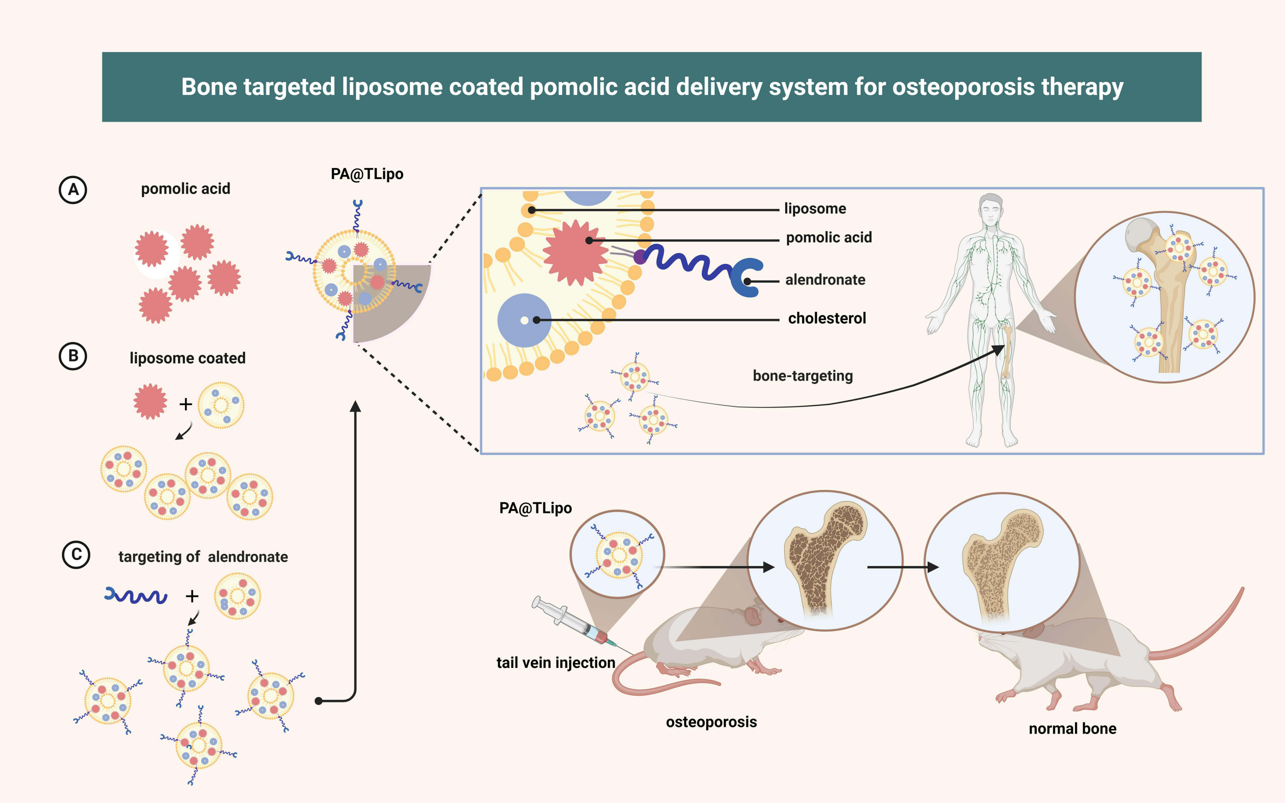

Figure 1 Schematic illustration of PA@TLipo and the underlying therapeutic role of osteoporosis.

obtained PA@TLipo exhibited excellent bone-targeting capability and could be easily internalized by bone marrow monocytes, thus effectively addressing the low bioavailability of PA. The results showed that PA@TLipo effectively inhibited osteoclast formation and bone resorption in vitro and reduced OVX-induced bone loss in vivo better than free PA. With the further development of aging population, the incidence of osteoporosis is increasing, which will bring huge pain to many elderly people. However, the PA@TLipo, this material has a clear effect on reducing bone loss, which will be a major discovery in the field of osteoporosis treatment. It has great clinical application potential and will bring good news to osteoporosis patients.

Materials and Methods

Materials

DSPE-PEG$_{3400}$-NHS, DSPC, Cholesterol, DSPE-mPEG2000 were purchased from Aladdin Industrial Corporation (Shanghai, China). Recombinant murine macrophage colony-stimulating factor (M-CSF) and RANKL were obtained from R&D Systems (Minneapolis, MN). Alpha Minimum essential medium (α-MEM) and fetal bovine serum (FBS) were purchased from HyClone (Logan, UT, United States). Cell Counting Kit-8 (CCK-8) and 1% penicillin/streptomycin were obtained from Beyotime (Shanghai, China). Tartrate-resistant acid phosphatase (TRAP) staining was acquired from Sigma-Aldrich (St. Louis, MO, United States).

Synthesis and Characterization of DSPE-PEG$_{3400}$-ALN

Based on the literature,[30] ALN-functionalized phospholipids were synthesized by an amidation reaction between DSPE-PEG$_{3400}$-NHS and ALN (Figure 2). Specifically, DSPE-PEG$_{3400}$-NHS and ALN were mixed in 0.1 M $NaHCO_3$ buffer (pH 8.5) at a molar ratio of 1:1.5. The mixture was sonicated in a water bath for 5 min followed by stirring at room temperature (RT) for 2 h. The mixture was purified via dialysis (1KDa, MWCO) in distilled water to remove free ALN. The final product was lyophilized and dissolved in $CDCl_3$ for ^{1}H NMR spectroscopy (Bruker AMX-600, Switzerland).

Preparation of PA@TLipo Nanoparticles

Liposomes encapsulating PA were prepared using the thin-film dispersion method. Briefly, 5 mg of DSPC, 1.24 mg of cholesterol, and 1.83 mg of DSPE-PEG$_{3400}$-ALN were dissolved in 4 mL chloroform/methanol (3:1, v/v) based on a molar ratio of 63:32:5 respectively. Subsequently, 1.6 mL of a PA methanol solution (1 mg/mL) was added to the above mixture according to a ratio of 20% relative to the total lipid content. Following by removing the organic solvents using a rotary evaporator, a lipid film was formed and subsequently hydrated with 6 mL sterile PBS for 30 min at 60 °C. The obtained coarse liposomes were sonicated in a water bath and extruded through a polycarbonate membrane with a 0.2 µm pore size (10 times). The resulting liposomes were purified using a Sephadex G50 spin column to remove the unencapsulated free PA. Nontargeted polyethylene glycol liposomes (PA@Lipo) were constructed using the same process as DSPE-mPEG$_{2000}$ instead of DSPE-PEG$_{3400}$-ALN. In addition, dye-labeled liposomes were prepared by adding DiD during lipid film formation.

Characterization of PA@TLipo Nanoparticles

The hydrodynamic particle size, zeta potential, and polydispersity index (PDI) of PA liposomes were determined using a Malvern dynamic light scattering (DLS) instrument (Zetasizer Pro). Briefly, the purified liposomes, dispersed in PBS at a concentration of 0.5 mg/mL, were subjected to size analysis. Importantly, prior to the assessment of the zeta potential, the liposome PBS solution (0.5 mg/mL) was dialyzed in distilled water. All measurements were conducted at 25 °C and were repeated three times. The morphology of PA liposomes was observed using transmission electron microscopy (TEM) (120 kV, JEM-1400 Flash, 120 kV). Briefly, the liposome solution was dropped onto a 200-mesh copper grid and incubated for 3 minutes. The liposomes were stained with 1 wt% phosphotungstic acid and dried before imaging. Colloidal stability of the PA liposomes was characterized using DLS. Briefly, the liposomes were dispersed in PBS solution containing 10% FBS and incubated at 37 °C with shaking (200 rpm). The particle sizes of liposomes were assessed at predetermined time intervals using a DLS instrument. In order to determine the drug loading capacity (DL) of PA within liposomes, the purified liposomes underwent lyophilization, and 2 mg of the resulting

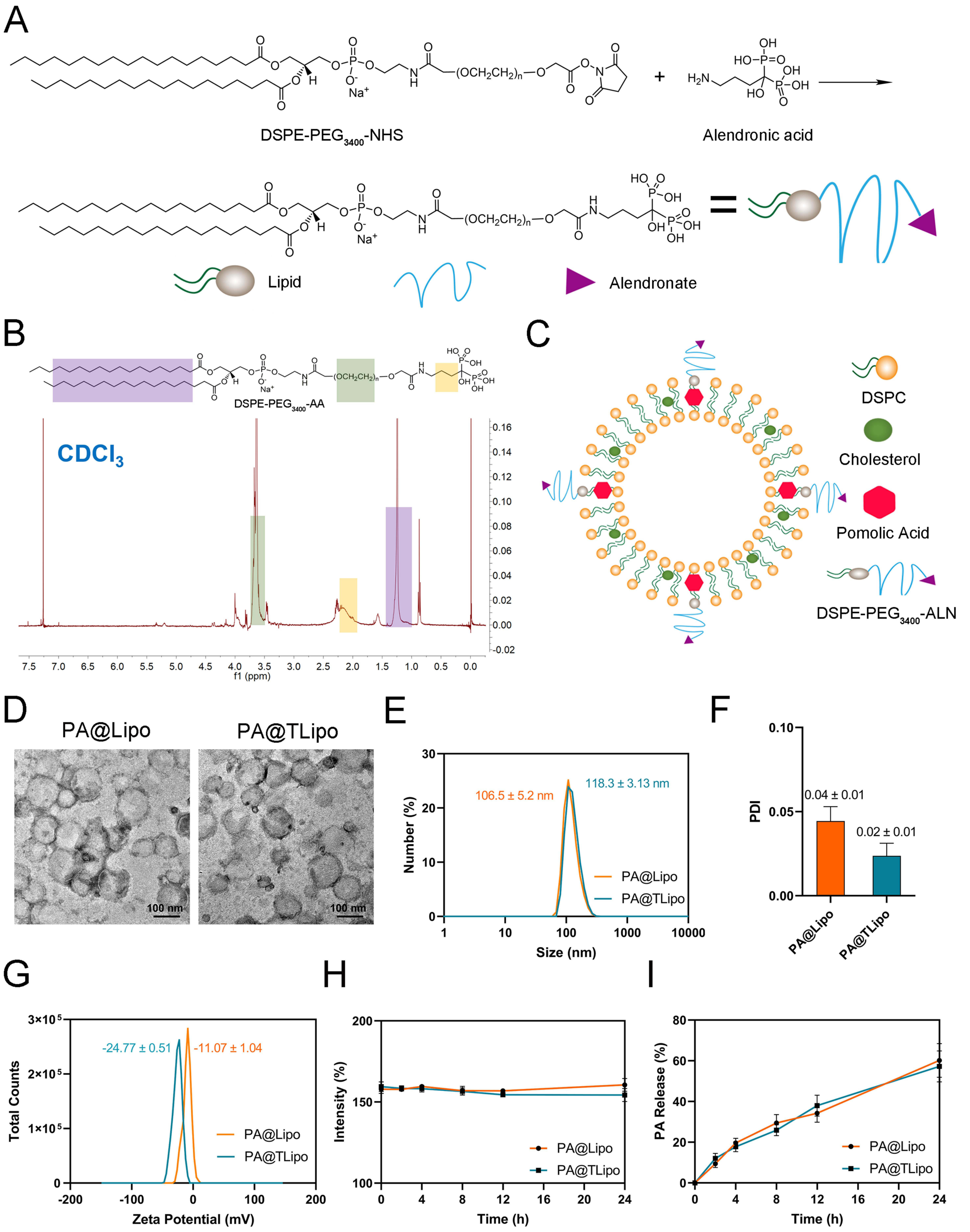

Figure 2 Synthesis and characterization of PA@TLipo and PA@Lipo. (**A**) Chemical synthesis of the DSPE-PEG$_{3400}$-ALN. (**B**) ^{1}HNMR characterization of DSPE-PEG$_{3400}$-ALN. (**C**) Schematic illustration of PA@TLipo prepared by thin-film hydration. (**D**) Representative TEM images of PA@TLipo and PA@Lipo (Scale bar = 100 nm). (**E**) Size, (**F**) PDI and (**G**) zeta potential of PA liposomes determined by DLS. (**H**) Colloidal stability of PA@TLipo and PA@Lipo in 10% FBS supplemented PBS at 37 °C during 24 h incubation. (**I**) Cumulative PA release in PBS (pH 7.4).

lyophilized powder (total mass of liposomes) was disrupted using 1 mL of methanol. Following this, the mass of PA encapsulated in liposomes was determined by using high-performance liquid chromatography (HPLC), employing absorption measurements at a wavelength of 210 nm. The standard curve for PA quantification was constructed using free PA. Briefly, 6 mL of freshly prepared PA-encapsulated liposomes were placed in the upper chamber of the Amicon® . Ultra centrifugal filter (100 kDa MWCO) before column purification and centrifuged at 3000 × g for 10 minutes. The liposomes collected in the upper chamber were resuspended in the original volume of PBS (6 mL) and subjected to three consecutive centrifugation cycles. The mass of PA in the filtrates was analyzed using HPLC after combining the three filtrates containing free PA. EE% was calculated as follow equation:

$$\mathrm{EE\%} = \frac{(\text{Total amount of PA during the preparation} - \text{Amount of free PA in filtrates})}{(\text{Total amount of PA during the preparation})} \times 100\%$$

Cell Culture and Cell Viability Assay

Primary bone marrow monocytes (BMMs) were obtained from the tibias and femurs in the C57BL/6J 4–6 week-old mice. Cells were cultured in α-MEM medium containing 10% FBS, 1% penicillin/streptomycin supplemented with 30 ng/mL M-CSF for four days, the attached cells were collected as BMMs for use in subsequent studies (Specific ethical guidelines are provided). BMMs (8×10^3 cells/well) were seeded overnight in 96-well plates. All the cells were subsequently treated with increasing concentrations of PA, PA@Lipo, or PA@TLipo (0, 6.25, 12.5, 25, 50, 100 μM) for 96 h. A 10 μL volume of CCK-8 reagent was administrated to each well. A Cytation 5 Cell Imaging Multi-Mode Reader (BioTek, Vermont, United States) was used to detect the absorbance of each well at 450 nm.

Osteoclastogenesis in vitro

BMMs (8×10^3 cells/well) were cultured in 96-well plates in complete α-MEM supplemented with 30 ng/mL M-CSF and 50 ng/mL RANKL. The cells were treated with PA, PA@Lipo, or PA@TLipo (12.5 μM). After treatment for 7 days, cells were then washed thrice with PBS, fixed with 4% paraformaldehyde (PFA) for 10 min, stained with TRAP solution at 37 °C for 30 min. Cells with at least three nuclei were classified as osteoclasts. Each well was imaged using a Cytation 5 Cell Imaging Multimode Reader.

Bone Resorption Assay

BMMs were seeded in 6-well plates at a density of 2×10^5 cells/well and stimulated with M-CSF and RANKL until small osteoclasts were formed. The cells were then digested and seeded onto hydroxyapatite-coated plates (8×10^3 cells/well) overnight. The adherent cells were treated with the indicated concentrations of PA, PA@Lipo, and PA@TLipo. After 4 days, cells were washed with 5% sodium hypochlorite solution, rinsed with sterile water, air-dried, and then captured using a Cytation 5 Cell Imaging Multi-Mode Reader. The area of bone resorption was measured using ImageJ software (National Institutes of Health, Bethesda, MD, USA).

Cellular Uptake Experiments

BMMs were seeded into a 96-well plate at a density of 8×10^3 cells/well and incubated for 24 h. The culture medium was then replaced with fresh medium containing DiD-labeled PA@Lipo, or DiD-labeled PA@TLipo (12.5 μM). After cultivation for 1, 2, and 4 h, the cells were washed thrice with cold PBS. Subsequently, the nuclei were stained with Hoechst33342, and intracellular fluorescence was observed using the Operetta CLS High Content Analysis System (PerkinElmer). (EX: 644 nm, EM: 665 nm).

OVX-Induced Osteoporosis Mouse Model

All animal studies were approved by the Institutional Animal Care and Ethics Committee of Shanghai University and animals used in this study were maintained in accordance with the Guideline for ethical review of animal welfare of laboratory animals published by the China National Standardization Management Committee (publication No. GB/T 35892–2018). 8-week-old C57BL/6 J female mice were purchased from Cavens Laboratory Animal (Changzhou, China).

The mice were randomly divided into five groups (n = 6) as follows: sham, OVX + PBS, OVX + 4 mg/kg PA, OVX +4 mg/kg PA@Lipo, and OVX +4 mg/kg PA@TLipo. After the mice were injected intraperitoneally with 3% chloral hydrate, bilateral ovariectomy was performed on the mice in the OVX group, OVX+4 mg/kg PA group, OVX+4 mg/kg PA@Lipo group, and OVX+4 mg/kg PA@TLipo group. After 1 week, the mice in the OVX+4 mg/kg PA, OVX+4 mg/kg PA@Lipo, and OVX+4 mg/kg PA@TLipo groups began to receive PA, PA@Lipo, or PA@TLipo via the tail vein every 2 days for 4 weeks.

Biophotonic Imaging Analysis

DiD-labeled PA@Lipo or PA@TLipo was administered to each mouse via tail vein. Thereafter, the mice were sacrificed at 4, 8, and 16 h (intravenous) after injection, and the major organs (heart, liver, spleen, lung, kidney, femur, and tibia) were harvested. The organs were visualized on a Quickview 3000 system (Bio-Real Sciences, Salzburg, Austria). The excitation and emission wavelengths were 644 nm and 665 nm, respectively.

Microcomputed Tomography (Micro-CT) Analyses

The femurs were fixed in 4% PFA for 24 h and then replaced with 75% alcohol. The structure and microarchitecture of the distal femur were obtained using a Skyscan 1275 mini-micro-CT scanner (BruKer, Karlsruhe, Germany) at (voltage of 70 kV, a current of 142 µA, and a resolution of 8 µm). The following bone-related parameters were analyzed: trabecular number (Tb.N, 1/mm), bone surface (BS, mm^2), bone volume/tissue volume (BV/TV, %), and trabecular separation (Tb.Sp, mm).

Histomorphometric Examination

For histological analysis, the femur was decalcified with EDTA decalcification solution (pH 7.4) for 3 weeks, dehydrated, paraffin-embedded, and sectioned using a microtome (4-µm thick sections). Hematoxylin-eosin staining (H&E) was used to visualize the bone microstructure of the femur, and TRAP staining was used to visualize osteoclasts.

Statistical Analyses

Data are expressed as mean ± standard deviation (Mean + SD) and were analyzed using GraphPad Prism 8.0.1 software (La Jolla, CA, USA). Differences between two groups were analyzed using the Student's *t*-tests, whereas differences between more than two groups were analyzed using two-way analysis of variance. $P < 0.05$ represent significant differences between the two groups of data.

Results

Synthesis and Characterization of Liposomes

To construct bone-targeted PA liposomes, ALN-conjugated phospholipids (DSPE-PEG$_{3400}$-ALN) were synthesized by an amidation reaction between NHS-group-functionalized phospholipids (DSPE-PEG$_{3400}$-NHS) and amine-containing ALN (Figure 2A). The chemical structure of DSPE-PEG$_{3400}$-ALN was confirmed using ^{1}H NMR (Figure 2B). The representative signal at 2.0 ppm corresponding to the CH$_2$ protons in ALN, was detected in the spectrum of DSPE-PEG$_{3400}$-ALN. The characteristic peaks at 1.26 ppm and 3.74 ppm correspond to the protons of the long hydrocarbon chain (CH$_2$) and the PEG's (CH$_2$O) in the DSPE-PEG$_{3400}$-NHS, respectively. The above data confirm the successful synthesis of DSPE-PEG$_{3400}$-ALN, which is consistent with a previous report.[31] PA liposomes were constructed using the thin-film hydration method, wherein DSPC, Cholesterol, and DSPE-PEG$_{3400}$-ALN were employed as constitutive membrane materials in a molar ratio of 63:32:5 (Figure 2C). Non-targeted liposomes (PA@Lipo) were prepared by replacing the DSPE-PEG$_{3400}$ -ALN component with DSPE-mPEG$_{2000}$. The particle size, zeta potential, and polydispersity index (PDI) of the PA liposomes were determined by dynamic light scattering (DLS). The hydrodynamic size of PA@Lipo was approximately 106 nm, which increased slightly to 118 nm for PA@TLipo (Figure 2E). The size distribution of both nanoformulations remained narrow, with a polydispersity index (PDI) below 0.1 (Figure 2F). The zeta potential of PA@Lipo and PA@TLipo nanoparticles were around −11.07±1.04 mV and −24.77±0.51 mV, respectively (Figure 2G). The higher negative charge observed on the surface of the PA@TLipo nanoparticles indicated successful modification of bone-targeted alendronate molecules onto the liposome surface. TEM images showed that the obtained PA@Lipo and PA@TLipo nanoparticles had a uniform morphology, and their sizes were consistent with the hydrodynamic diameter (Figure 2D). Both PA@Lipo and PA@TLipo nanoparticles demonstrated good colloidal stability in PBS solution containing 10% FBS at 37 °C for 24 h (Figure 2H). The DL of PA in PA@Lipo and PA@TLipo was approximately 14.5% and 13%, respectively, when drug-to-lipid ratio of 1:5 was employed. Additionally, the encapsulation efficiency (EE%) of PA in PA@Lipo and PA@TLipo was approximately 72% and 71%, respectively. Cumulative PA release in PBS (pH 7.4) exhibited minimal differences between PA@Lipo and PA@TLipo nanoparticles (Figure 2I).

Cell Uptake Capability of PA@TLipo and Its Effects on Osteoclast Formation and Bone Resorption in vitro

PA and PA-loaded liposome nanoparticles (0, 6.25, 12.5, 25, 50, and 100 μM) were cultured in BMMs for 96 h and cytotoxicity was detected using CCK-8. Figure 2 shows that PA-loaded liposome nanoparticles (PA@Lipo and PA@TLipo) reduced the toxic effect on BMMs and improved the biocompatibility of PA compared to free PA when the concentration was higher than 50 μM (Figure 3A). No significant difference was observed in the cytotoxic effects of PA@TLipo and PA@Lipo on BMMs. To evaluate the cellular uptake, DiD labeled PA@TLipo was incubated with BMMs for 1, 2, and 4 h. The fluorescence intensity of PA@Lipo-treated cells was low at first, but reached the highest level at 4 h. There was no significant difference in cellular uptake between PA@TLipo and PA@Lipo in BMMs (Figure 3B). These results indicated that bone-targeted alendronate molecules modified on the surface of nanoparticles did not affect cellular uptake by BMMs.

We examined the effects of PA@TLipo on RANKL-induced osteoclast formation and bone resorption in vitro. After induction with M-CSF and RANKL, PA@TLipo group (12.5μM) significantly diminished the number of TRAP-positive osteoclasts (nuclei ≥ 3, Figure 3C) and area of bone resorption pits compared with the other groups (Figure 3D). These results suggested that PA@TLipo inhibited osteoclast formation and bone resorption.

Bone-Targeted Capability and Compatibility of PA@TLipo

The bone targeting ability of PA@TLipo was further investigated in vivo. Female C57BL/6 mice were intravenously injected with DiD-labeled PA@TLipo and DiD-labeled PA@Lipo. To evaluate biodistribution, the organs (heart, liver, lung, spleen, kidney, femur, and tibia) were excised and used for an in vivo imaging. Fluorescence signal intensity was calculated for quantification. The fluorescence intensity in the femur and tibia of the PA@TLipo group showed a gradually increasing trend from 4 h to 8 h. The fluorescence signals in the tibia and femur of the PA@TLipo group were much stronger than those in the PA@Lipo group at each time point (Figure 4A). At 8 h, the strongest fluorescence intensity was observed in the tibias and femurs of the PA@TLipo group. After 16 h, the fluorescence intensity was maintained at a high level in the PA@TLipo group, but little residual fluorescence was detected in the femur and tibia of the PA@Lipo group, suggesting that alendronate modification facilitated bone-targeting capability of liposomes and prolonged their retention time in the bone.

After continuous intravenous administration, H&E staining of the main organs, including the heart, liver, spleen, lung, and kidney, was examined. All the treatment groups exhibited similar histological morphologies, which validated the good biocompatibility of PA@TLipo (Figure 4B). In conclusion, we successfully constructed a bone-targeted PA@TLipo without inducing systemic toxicity.

PA@TLipo Attenuates Bone Loss in OVX Mice

Therefore, we investigated the therapeutic effects of PA@TLipo on OVX-induced bone loss in mice. Mice were separated into five groups: sham, OVX, PA, PA@Lipo, and PA@TLipo. Micro-CT analysis revealed that OVX-induced bone loss was completely prevented by PA@TLipo treatment (Figure 5A). Quantitative analysis showed that PA@TLipo administration in OVX mice significantly increased the Tb. N, BS, and BV/TV and decreased Tb. Sp (Figure 5B). Consistently, PA@TLipo attenuated OVX-induced bone loss as observed by H&E staining

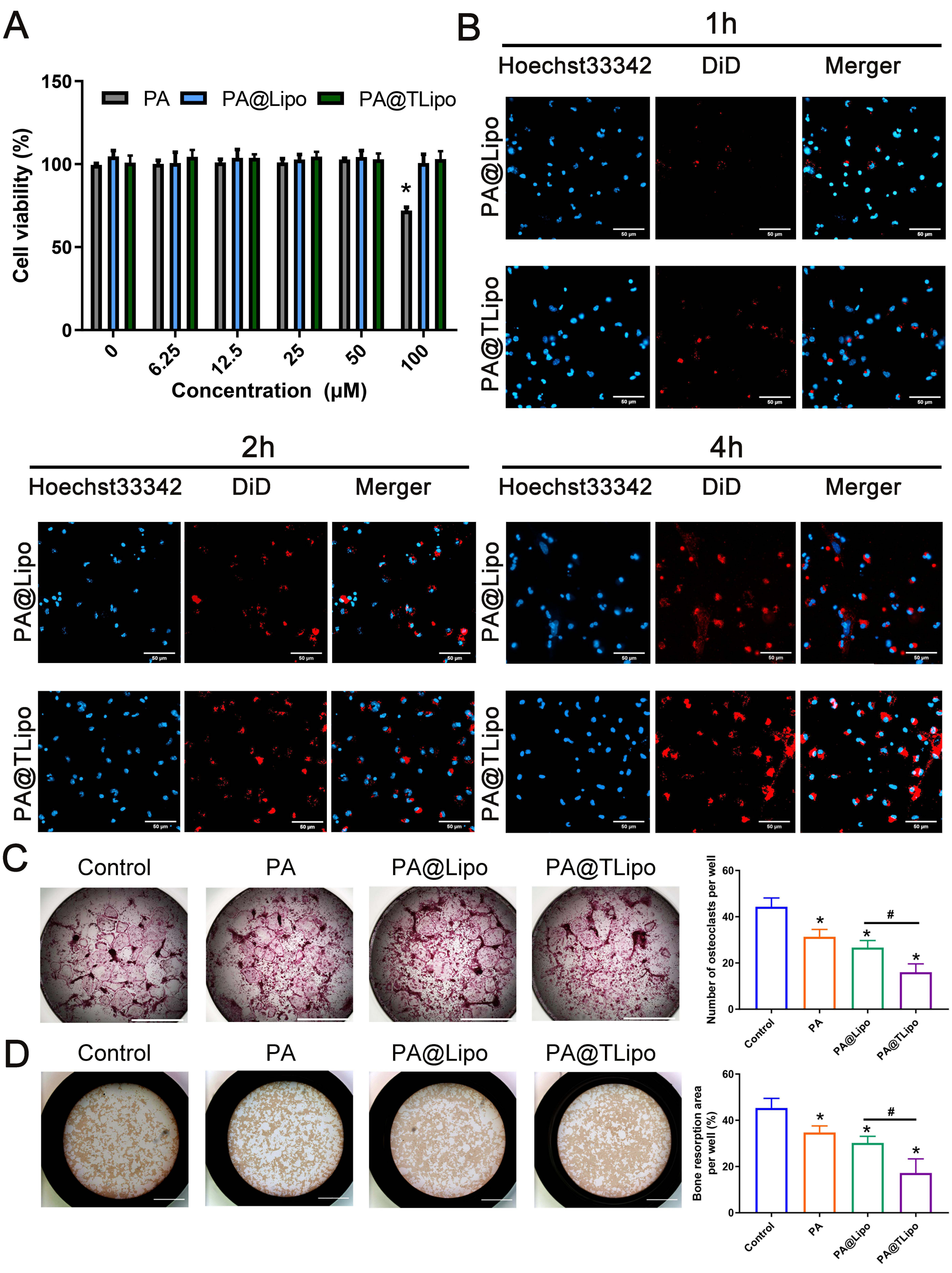

Figure 3 The cellular uptake of PA@TLipo and its effects on osteoclast formation and bone resorption in BMMs. (**A**) Cell viability of BMMs co-cultured with indicated concentrations of PA, PA@Lipo, or PA@TLipo (0, 6.25, 12.5, 25, 50, 100 μM) for 96 h by CCK-8 assay (n = 3). $^{*}P < 0.05$ compared with the control. (**B**) Cellular uptake in BMMs incubated with DiD labeled PA@Lipo and PA@TLipo for 1, 2, and 4 h, respectively. Red: DiD labeled PA@Lipo and PA@TLipo; blue: Hoechst33342 stained cell nucleus. Scale bar = 50 μm. (**C**) BMMs were stimulated with RANKL in the presence of PA, PA@Lipo, or PA@TLipo (12.5 μM) and measured by TRAP staining. TRAP-positive multinucleated (nuclei ≥ 3) cells was quantified (n = 3). Scale bar = 2000 μm. $^{*}P < 0.05$ in contrast with the control. $^{\#}P < 0.05$ relative to the PA@Lipo group. (**D**) Bone resorption pits assay in different groups and the area of resorption pits were quantified using Image J (n = 3). All bar graphs are presented as the mean ± SD. Scale bar = 2000 μm. $^{*}P < 0.05$ compared to the control. $^{\#}P < 0.05$ relative to the PA@Lipo group.

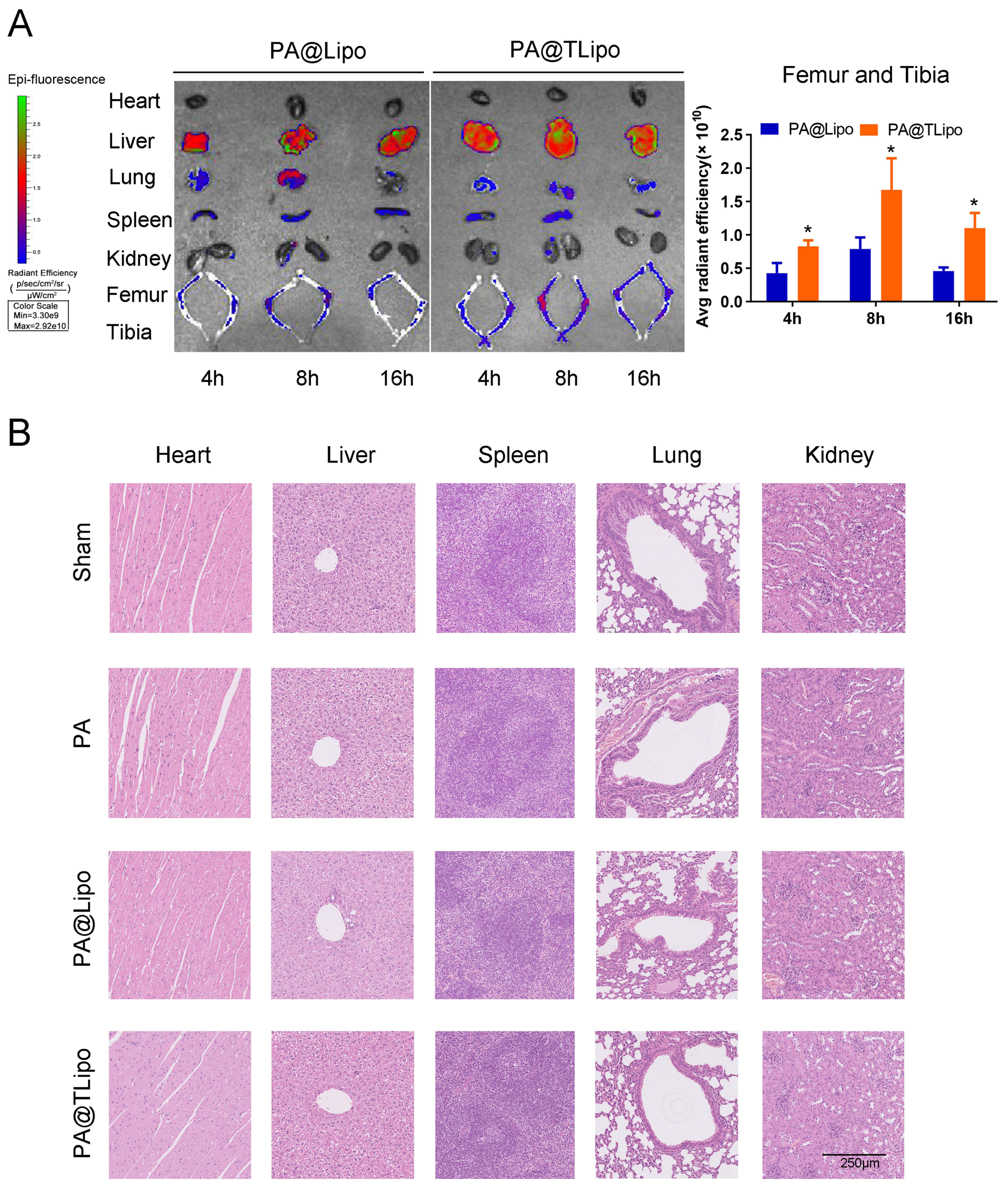

Figure 4 In vivo distribution and toxicity assay of PA@TLipo. (**A**) Fluorescence images of the major organs (heart, liver, lung, spleen, kidney, femur and tibia) of mice after tail vein injection of DiD-labeled PA@Lipo and PA@TLipo at 4 h, 8 h, and 16h, respectively. Fluorescence intensity quantification of femurs and tibias (n = 3). $^*P < 0.05$ in contrast with the PA@Lipo group. (**B**) H&E staining of organs (heart, liver, spleen, lung, and kidney) after tail vein injection of PA, PA@Lipo, and PA@TLipo. Scale bar = 250 µm.

(Figure 5C and D). TRAP staining showed that PA@TLipo remarkably diminished the TRAP-positive cell count around the trabecula compared with that in the OVX group (Figure 5E and F). PA@TLipo demonstrated greater efficacy in inhibiting bone loss compared to the PA@Lipo treatment, possibly due to the alendronate modification,

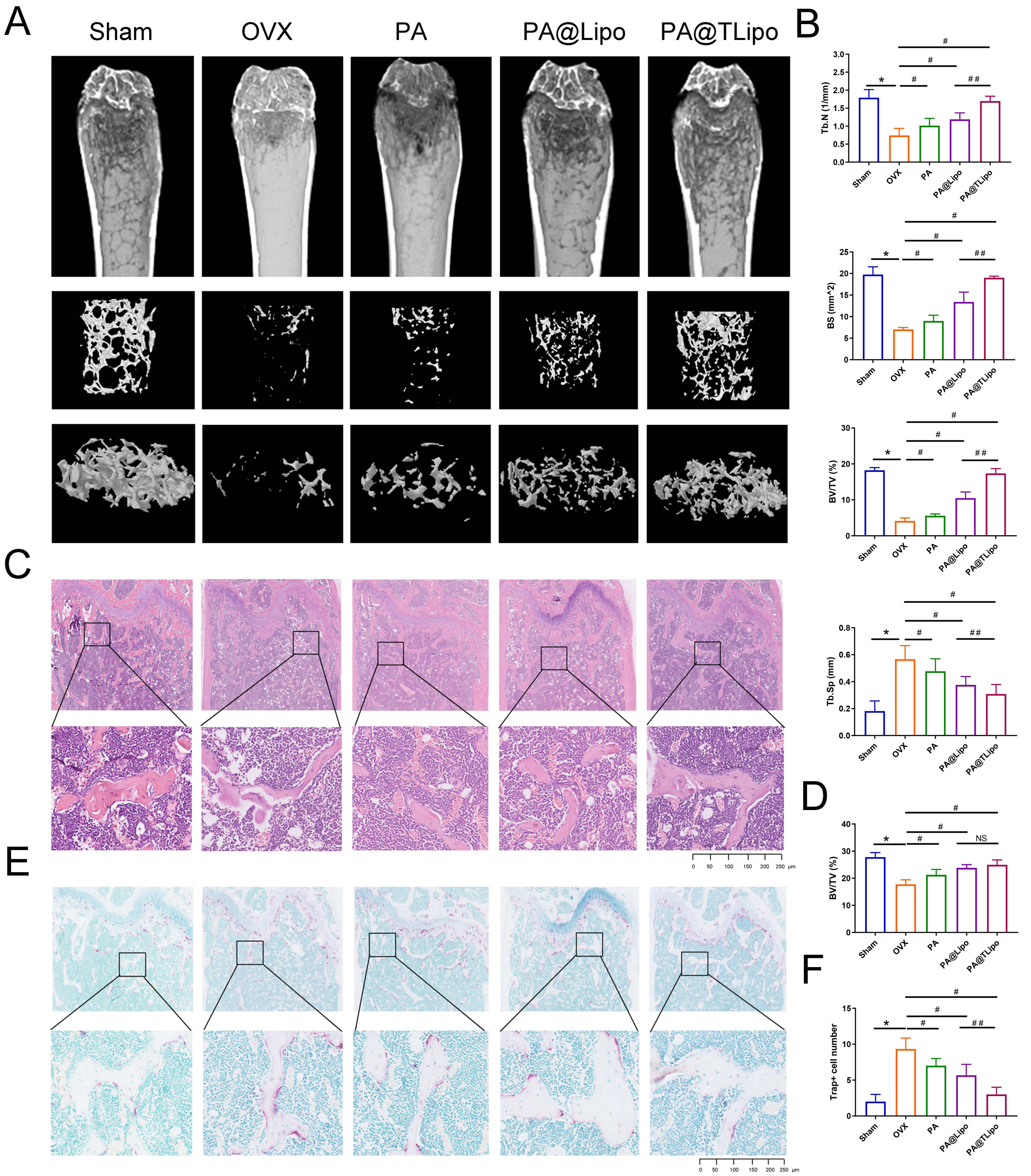

Figure 5 PA@TLipo ameliorates OVX-induced bone loss in vivo. (**A**) Micro CT analysis of the distal femur from sham, OVX with PBS injection (OVX), OVX with PA (4 mg/kg), OVX with PA@Lipo (4 mg/kg), and OVX with PA@TLipo (4 mg/kg). (**B**) Quantification of Tb. N, BS, BV/TV, and Tb. Sp. The results represent the means ± SD (n = 6). $^{*}P < 0.05$ in contrast with the sham group. $^{\#}P < 0.05$ versus the PBS-treated OVX group. $^{\#\#}P < 0.01$ versus the PA@Lipo group. (**C**) Representative histological images of distal femoral sections after H&E staining. Scale bar = 250 μm. (**D**) The graph bars show the quantitative results of BV/TV. NS, no significant difference. (**E**) Representative images of TRAP staining of the femurs in each groups were shown. (**F**) The number of TRAP (+) osteoclasts on the trabecular bone surface was shown in the bar graph. Scale bar = 250 μm. Data were presented as mean ± SD. $^{*}P < 0.05$ in contrast with the sham group. $^{\#}P < 0.05$ versus the PBS-treated OVX group. $^{\#\#}P < 0.01$ versus the PA@Lipo group.

which enhances the targeted delivery of PA to the bone. Collectively, these results suggested that PA@TLipo repressed osteoclast formation and rescued OVX-induced bone loss.

Discussion

Bone homeostasis is coordinated by osteoclast-mediated bone resorption and osteoblast-induced bone formation.[32,33] Excessive osteoclast activity disrupts bone homeostasis, leading to severe osteoporosis.[34] The incidence of fractures due to osteoporosis has been increasing over the last decade, seriously threatening the life and health of patients.[35] With the aging of the population increasing annually, the proportion of menopausal women is also increasing. Therefore, it is particularly important to solve the problem of osteoporosis. Current clinical therapies, such as bisphosphonates or denosumab, are effective but have long-term side effects, including atypical femoral fractures.[36] Thus, the search for new drugs with minor side effects is imperative in osteoporosis treatment.

Salvia miltiorrhiza has been widely used in Asia as a compound for the treatment of osteoporosis.[37] In our previous study, we constructed a Salvia miltiorrhiza chemical component database using network-pharmacological methods. Using this database, we calculated the average similarity scores of the candidate compounds and selected five candidate compounds based on their rankings for further biological activity experiments. The results showed that Salvia miltiorrhiza triterpenoid PA significantly inhibited RANKL-induced osteoclast differentiation and bone resorption, and attenuated OVX-induced osteoporosis by repressing osteoclast activity. These results laid the foundation for this study. However, we also found that many problems still need to be resolved. PA, a triterpenoid monomer of Salvia divinorum, has strong pharmacological effects, poor water solubility, and a lack of bone targeting, limiting its clinical application. Therefore, the development of a bone-targeting drug delivery system that delivers PA to the bones is an ideal strategy. This targeting and good solubility are also necessary for efficient clinical application. At the beginning of its design, liposomes were used as drug carriers in the field of medicine, because liposomes were designed with phospholipids as membrane materials, and phospholipids were the basic materials to form the bilayer of liposomes,[38,39] therefore, the liposome is similar to the cell membrane, so it has a strong affinity between the liposome and the cell membrane. It can penetrate the cell membrane well and act on the cell itself with good biocompatibility. Therefore, we synthesized PA@TLipo, which was more easily absorbed by cells after liposome encapsulation than pure PA. In this study, we modified liposomes with ALN to design an advanced drug delivery system that can direct PA to bone tissue, which shows great advantages in improving drug safety, therapeutic efficacy and precision combination therapy.

First, to solve the problem of solubility, we used liposomes as the wrapping material for PA. Liposomes are commonly used as ideal nanocarriers owing to their tolerability and biosafety, and they can fuse with cell membranes. Therefore, in the biomedical field, they are often used for the encapsulation and delivery of drugs, as demonstrated in several previous studies.[40,41] In addition to tolerability and overall safety, liposomes have been reported to increase drug absorption, decreasing drug toxicity, overcoming barriers to cellular and tissue uptake, as well as promoting the distribution of drugs to the target site in vivo.[42,43] Due to the lack of targeting of PA, we have also made corresponding improvements: as a bone-targeted modifier, ALN chelates prepared with anti-osteoporosis drugs could correct the poor specificity and adverse reactions of the original drug.[44] However, bone-targeted therapy for osteoporosis has always attracted attention. Among them, BT-Exo-siShn3 bone-targeting system mainly acts on osteoblasts[45] and clearly has the effect of increasing bone mass, while PA@TLipo mainly targets osteoclasts and can modulate bone loss. In contrast, bioinspired BMEC-targeting nanovesicles[46] and bone-targeted biomimetic nanogels[47] also have targeting effects and are similar to PA@TLipo in terms of drug encapsulation. This also represents the increasing attention paid to the targeted therapy of osteoporosis, and there is still a good research scene in this field.

Thus, we selected ALN as the bone-targeted molecule and incorporated it into the liposome membrane as the targeting head to form a bone-targeted delivery system. We coated PA with liposomes and added ALN, a substance that can bind specifically to bone, to the surface of the lipid and synthesized PA@TLipo through the above procedures. The safety of this material and its effects on osteoclasts were confirmed in vitro. We further studied the effects of a bone-targeted delivery system with PA in OVX mice in vivo. Analysis of micro-CT scanning indicated that targeting the delivery system with PA could effectively reverse bone loss, as evidenced by the significant attenuation of Tb. Sp and an increase in the bone mass index. TRAP staining following bone hematoxylin and eosin staining further demonstrated that targeting the delivery system with PA significantly reduced the number of osteoclasts in the trabecular region. Furthermore, in terms of the targeting of materials, we carried out more in-depth research, and the data from biophotonic imaging in vivo validated that DiD-labeled bone-targeted liposomes could deliver PA encapsulated in liposomes to certain bone tissues and reduce the exposure of PA to non-bone tissues, and that the fluorescence signal was significantly stronger in bone tissue and relatively lower in non-bone tissue. These results provided a foundation for the application of this material in the field of osteoporosis.

After in-depth analysis of this material, we found that ALN is a drug approved by the US Food and Drug Administration (FDA) for the treatment of osteoporosis.[48] In the clinical application process, ALN has strong functions and advantages in increasing bone mineral density of the femur and lumbar spine.[49] With the deepening of research, scholars have gradually found that due to its strong bone affinity, it is often modified on the surface of drugs to enhance bone targeting.[50] In this study, ALN can not only assist the targeted action of traditional Chinese medicine monomers on bone tissue, but also have the effect of anti-osteoporosis itself, and its dual effect cannot be ignored. This dual function is one of the core points of its future clinical application. What's more, the targeting property of ALN is also the key point of its clinical application and the biocompatibility of liposomes also reduce the adverse reactions of PA@TLipo. Our research aims to provide ideas for the treatment of osteoporosis, and PA@TLipo. It has shown significant advantages in this regard, especially in inhibiting osteoclasts. Our study lays the foundation for the application of PA@TLipo in the field of osteoporosis. This may provide a solution for osteoporosis. Therefore, we believe that in the future, through more in-depth mechanism research, PA@TLipo. It will bring good news to patients with osteoporosis.

Conclusion

In this study, a novel therapeutic agent was designed and constructed to treat osteoporosis, consisting of a liposome material as the core and drug pocket, PA as the anti-osteoporosis drug, and ALN as the bone-targeting molecule. Cellular analyses showed that a bone-targeted delivery system with PA effectively inhibited osteoclast differentiation and bone resorption. Moreover, the bone-targeted delivery system with PA showed rapid cellular uptake by BMMs and good biocompatibility, with less cytotoxic effects. In particular, in vivo experiments showed that the targeted delivery system could reverse OVX-induced osteoporosis and maintained the bone microstructure in OVX mice with low toxicity to major organs. To the best of our knowledge, this study is the first to employ a bone-targeted delivery system to deliver PA for OVX-induced bone loss, providing an innovative solution for treating osteoporosis.

Acknowledgments

This work was supported by grants from the National Natural Science Foundation of China (82104220), Nature Science Foundation of Hainan (823QN254), Natural Science Foundation of Shanghai (21ZR1449200), Yangfan Project of Science and Technology Commission of Shanghai Municipality (22YF1427500), International Cooperation Project of Science and Technology Commission of Shanghai Municipality (22430710900), National Natural Science Foundation of China (82303798), and Natural Science Research Project of Shanghai Minhang District (2020MHZ022).

Author Contributions

All authors made a significant contribution to the work reported, whether that is in the conception, study design, execution, acquisition of data, analysis and interpretation, or in all these areas; took part in drafting, revising or critically reviewing the article; gave final approval of the version to be published; have agreed on the journal to which the article has been submitted; and agree to be accountable for all aspects of the work.

Disclosure

The authors declare that they have no conflicts of interest in this work.

References

1. Aspray TJ, Hill TR. Osteoporosis and the ageing skeleton. *Sub Cell Biochem*. 2019;91:453–476. doi:10.1007/978-981-13-3681-2_16
2. Ensrud KE, Crandall CJ. Osteoporosis. *Ann Internal Med*. 2017;167(3):Itc17–Itc32. doi:10.7326/aitc201708010

3. Zhao X, Patil S, Xu F, Lin X, Qian A. Role of biomolecules in osteoclasts and their therapeutic potential for osteoporosis. *Biomolecules*. 2021;11 (5). doi:10.3390/biom11050747
4. Kandel R, Jang SR, Shrestha S, et al. Biomimetic cell-substrate of chitosan-cross-linked polyaniline patterning on TiO(2) nanotubes enables hBM-MSCs to differentiate the osteoblast cell type. *ACS Appl Mater Interfaces*. 2021;13(39):47100–47117. doi:10.1021/acsami.1c09778
5. Ghimire U, Kandel R, Ko SW, Adhikari JR, Kim CS, Park CH. Electrochemical technique to develop surface-controlled polyaniline nano-tulips (PANINTs) on PCL-reinforced chitosan functionalized (CS-f-Fe(2)O(3)) scaffolds for stimulating osteoporotic bone regeneration. *Int J Biol Macromol*. 2024;264(Pt 1):130608. doi:10.1016/j.ijbiomac.2024.130608
6. Kandel R, Jang SR, Ghimire U, et al. Engineered nanostructure fibrous cell-laden biointerfaces integrating Fe3O4/SrO2-fMWCNTs induce osteogenesis and anti-bacterial effect. *J Ind Eng Chem*. 2023;120:216–230. doi:10.1016/j.jiec.2022.12.028
7. Ayers C, Kansagara D, Lazur B, Fu R, Kwon A, Harrod C. Effectiveness and safety of treatments to prevent fractures in people with low bone mass or primary osteoporosis: a living systematic review and network meta-analysis for the American College of Physicians. *Ann Internal Med*. 2023;176(2):182–195. doi:10.7326/m22-0684
8. Tella SH, Gallagher JC. Prevention and treatment of postmenopausal osteoporosis. *J Steroid Biochem Mol Biol*. 2014;142:155–170. doi:10.1016/j.jsbmb.2013.09.008
9. Reid IR, Billington EO. Drug therapy for osteoporosis in older adults. *Lancet*. 2022;399(10329):1080–1092. doi:10.1016/s0140-6736(21)02646-5
10. Khosla S, Hofbauer LC. Osteoporosis treatment: recent developments and ongoing challenges. *Lancet Diabetes Endocrinol*. 2017;5(11):898–907. doi:10.1016/s2213-8587(17)30188-2
11. Martiniakova M, Babikova M, Omelka R. Pharmacological agents and natural compounds: available treatments for osteoporosis. *J Physiol Pharmacol*. 2020;71(3). doi:10.26402/jpp.2020.3.01
12. Aljohani S, Fliefel R, Ihbe J, Kühnisch J, Ehrenfeld M, Otto S. What is the effect of anti-resorptive drugs (ARDs) on the development of medication-related osteonecrosis of the jaw (MRONJ) in osteoporosis patients: a systematic review. *J Craniomaxillofac Surg*. 2017;45 (9):1493–1502. doi:10.1016/j.jcms.2017.05.028
13. Zhang J, Zhang Q, Liu G, Zhang N. Therapeutic potentials and mechanisms of the Chinese traditional medicine Danshensu. *Eur J Pharmacol*. 2019;864:172710. doi:10.1016/j.ejphar.2019.172710
14. Zhang Z, He H, Qiao Y, et al. Tanshinone IIA pretreatment protects H9c2 cells against Anoxia/Reoxygenation injury: involvement of the translocation of Bcl-2 to mitochondria mediated by 14-3-3η. *Oxid Med Cell Longev*. 2018;2018:3583921. doi:10.1155/2018/3583921
15. Li S, Duan S, Ning Y, Zhang H, Zheng Q. Efficacy and safety of Danhong injection on endothelial function and inflammatory factors after the percutaneous coronary intervention for coronary heart disease: a protocol of systematic review and meta-analysis of randomized controlled trials. *Medicine*. 2020;99(27):e20783. doi:10.1097/md.0000000000020783
16. Ma Y, Cui G, Chen T, et al. Expansion within the CYP71D subfamily drives the heterocyclization of tanshinones synthesis in Salvia miltiorrhiza. *Nat Commun*. 2021;12(1):685. doi:10.1038/s41467-021-20959-1
17. Sun C, Cui L, Zhou B, Wang X, Guo L, Liu W. Visualizing the spatial distribution and alteration of metabolites in continuously cropped Salvia miltiorrhiza Bge using MALDI-MSI. *J Pharm Anal*. 2022;12(5):719–724. doi:10.1016/j.jpha.2021.09.011
18. Tang Y, Wa Q, Peng L, et al. Salvianolic acid B suppresses ER stress-induced NLRP3 inflammasome and pyroptosis via the AMPK/FoxO4 and Syndecan-4/Rac1 signaling pathways in human endothelial progenitor cells. *Oxid Med Cell Longev*. 2022;2022:8332825. doi:10.1155/2022/8332825
19. Tang F, Wang Z, Zhou J, Yao J. Salvianolic acid A protects against acetaminophen-induced hepatotoxicity via regulation of the miR-485-3p/SIRT1 Pathway. *Antioxidants*. 2023;12(4). doi:10.3390/antiox12040870
20. Yen JH, Huang ST, Huang HS, et al. HGK-sestrin 2 signaling-mediated autophagy contributes to antitumor efficacy of Tanshinone IIA in human osteosarcoma cells. *Cell Death Dis*. 2018;9(10):1003. doi:10.1038/s41419-018-1016-9
21. Guan Y, Li L, Kan L, Xie Q. Inhalation of salvianolic acid B prevents fine particulate matter-induced acute airway inflammation and oxidative stress by downregulating the LTR4/MyD88/NLRP3 pathway. *Oxid Med Cell Longev*. 2022;2022:5044356. doi:10.1155/2022/5044356
22. Leng X, Kan H, Wu Q, Li C, Zheng Y, Peng G. Inhibitory effect of Salvia miltiorrhiza extract and its active components on cervical intraepithelial neoplastic cells. *Molecules*. 2022;27(5):1582.
23. Li ZM, Xu SW, Liu PQ. Salvia miltiorrhizaBurge (Danshen): a golden herbal medicine in cardiovascular therapeutics. *Acta Pharmacol Sin*. 2018;39(5):802–824. doi:10.1038/aps.2017.193
24. Lee SR, Jeon H, Kwon JE, et al. Anti-osteoporotic effects of Salvia miltiorrhiza Bunge EtOH extract both in ovariectomized and naturally menopausal mouse models. *J Ethnopharmacol*. 2020;258:112874. doi:10.1016/j.jep.2020.112874
25. Lai W, Mo Y, Wang D, et al. Tanshinol alleviates microcirculation disturbance and impaired bone formation by attenuating TXNIP signaling in GIO rats. *Front Pharmacol*. 2021;12:722175. doi:10.3389/fphar.2021.722175
26. Yang W, Han J, Gong S, Zhao J, Yu T, Ma J. Cryptotanshinone suppressed postmenopausal osteoporosis by preventing RANKL-mediated osteoclastogenesis against kidney injury. *Evid Based Complement Alternat Med*. 2022;2022:2821984. doi:10.1155/2022/2821984
27. Ekeuku SO, Pang KL, Chin KY. The skeletal effects of tanshinones: a review. *Molecules*. 2021;26(8). doi:10.3390/molecules26082319
28. Ma C, Mo L, Wang Z, et al. Dihydrotanshinone I attenuates estrogen-deficiency bone loss through RANKL-stimulated NF-κB, ERK and NFATc1 signaling pathways. *Int Immunopharmacol*. 2023;123:110572. doi:10.1016/j.intimp.2023.110572
29. Chen G, Zhang X, Lin H, Huang G, Chen Y, Cui L. Tanshinol alleviates osteoporosis and myopathy in glucocorticoid-treated rats. *Planta med*. 2017;83(16):1264–1273. doi:10.1055/s-0043-108761
30. Li J, Zhang R, Du Y, et al. Osteophilic and dual-regulated alendronate-gene lipoplexes for reversing bone loss. *Small*. 2023;19(45):e2303456. doi:10.1002/smll.202303456
31. Chen Q, Zheng C, Li Y, et al. Bone targeted delivery of SDF-1 via alendronate functionalized nanoparticles in guiding stem cell migration. *ACS Appl Mater Interfaces*. 2018;10(28):23700–23710. doi:10.1021/acsami.8b08606
32. Kim JM, Lin C, Stavre Z, Greenblatt MB, Shim JH. Osteoblast-osteoclast communication and bone homeostasis. *Cells*. 2020;9(9). doi:10.3390/cells9092073
33. Tuckermann J, Adams RH. The endothelium-bone axis in development, homeostasis and bone and joint disease. *Nat Rev Rheumatol*. 2021;17 (10):608–620. doi:10.1038/s41584-021-00682-3
34. Omi M, Mishina Y. Roles of osteoclasts in alveolar bone remodeling. *Genesis*. 2022;60(8–9):e23490. doi:10.1002/dvg.23490

35. Vogelsang EM, Raymo JM, Liang J, Kobayashi E, Fukaya T. Population aging and health trajectories at older ages. *J Gerontol B Psychol Sci Soc Sci*. 2019;74(7):1245–1255. doi:10.1093/geronb/gbx071
36. Kobayakawa T, Miyazaki A, Saito M, Suzuki T, Takahashi J, Nakamura Y. Denosumab versus romosozumab for postmenopausal osteoporosis treatment. *Sci Rep*. 2021;11(1):11801. doi:10.1038/s41598-021-91248-6
37. Lin J, Zhu J, Wang Y, et al. Chinese single herbs and active ingredients for postmenopausal osteoporosis: from preclinical evidence to action mechanism. *Biosci Trends*. 2017;11(5):496–506. doi:10.5582/bst.2017.01216
38. Has C, Sunthar P. A comprehensive review on recent preparation techniques of liposomes. *J Liposome Res*. 2020;30(4):336–365. doi:10.1080/08982104.2019.1668010
39. Fenske DB, Cullis PR. Liposomal nanomedicines. *Expert Opin Drug Delivery*. 2008;5(1):25–44. doi:10.1517/17425247.5.1.25
40. Guimarães D, Cavaco-Paulo A, Nogueira E. Design of liposomes as drug delivery system for therapeutic applications. *Int J Pharm*. 2021;601:120571. doi:10.1016/j.ijpharm.2021.120571
41. Dymek M, Sikora E. Liposomes as biocompatible and smart delivery systems - The current state. *Adv Colloid Interface Sci*. 2022;309:102757. doi:10.1016/j.cis.2022.102757
42. Abu Lila AS, Ishida T. Liposomal delivery systems: design optimization and current applications. *Biol Pharm Bull*. 2017;40(1):1–10. doi:10.1248/bpb.b16-00624
43. Almeida B, Nag OK, Rogers KE, Delehanty JB. Recent progress in bioconjugation strategies for liposome-mediated drug delivery. *Molecules*. 2020;25(23). doi:10.3390/molecules25235672
44. Klara J, Lewandowska-łańcucka J. How efficient are alendronate-nano/biomaterial combinations for anti-osteoporosis therapy? An evidence-based review of the literature. *Int j Nanomed*. 2022;17:6065–6094. doi:10.2147/ijn.S388430
45. Cui Y, Guo Y, Kong L, et al. A bone-targeted engineered exosome platform delivering siRNA to treat osteoporosis. *Bioact Mater*. 2022;10:207–221. doi:10.1016/j.bioactmat.2021.09.015
46. Cui Y, Li Z, Guo Y, et al. Bioinspired nanovesicles convert the skeletal endothelium-associated secretory phenotype to treat osteoporosis. *ACS nano*. 2022;16(7):11076–11091. doi:10.1021/acsnano.2c03781
47. Cui Y, Lv B, Li Z, et al. Bone-targeted biomimetic nanogels re-establish osteoblast/osteoclast balance to treat postmenopausal osteoporosis. *Small*. 2024;20(6):e2303494. doi:10.1002/smll.202303494
48. Iwamoto J, Takeda T, Sato Y. Efficacy and safety of alendronate and risedronate for postmenopausal osteoporosis. *Curr Med Res Opin*. 2006;22(5):919–928. doi:10.1185/030079906x100276
49. Radwan A, Shraim N, Elaraj J, et al. Knowledge and compliance towards alendronate therapy among postmenopausal women with osteoporosis in Palestine. *BMC Women's Health*. 2022;22(1):105. doi:10.1186/s12905-022-01690-5
50. Krüger TB, Syversen U, Herlofson BB, Lian AM, Reseland JE. Targeting a therapeutically relevant concentration of alendronate for in vitro studies on osteoblasts. *Acta Odontol Scand*. 2022;80(8):619–625. doi:10.1080/00016357.2022.2072522